A Numerical Model to Study the Nonlinear and Unsteady Aerodynamics of Bioinspired Morphing-Wing Concepts

Marcos L. Verstraete, Sergio Preidikman, Bruno A. Roccia and Dean T. Mook

Reprinted from

International Journal of
Micro Air Vehicles

Volume 7 · Number 3 · September 2015

Multi-Science Publishing
ISSN 1756-8293

A Numerical Model to Study the Nonlinear and Unsteady Aerodynamics of Bioinspired Morphing-Wing Concepts

Marcos L. Verstraete[1,2], Sergio Preidikman[2], Bruno A. Roccia[1,2] and Dean T. Mook[3]

[1]Mechanical Engineering Department, Engineering School, Universidad Nacional de Río Cuarto, Argentina. verstraete.ml@gmail.com

[2]Department of Structures, School of Exact, Physical and Natural Sciences. Universidad Nacional de Córdoba, Argentina. spreidik@umd.edu, broccia@ing.unrc.edu.ar

[3]Virginia Polytechnic Institute and State Univ., Blacksburg, VA, USA. dtmook@vt.edu

ABSTRACT

In the present paper, a numerical model to study the nonlinear and unsteady aerodynamics of morphing-wing concepts inspired by bird flight is developed. The model includes: *i*) a wing topology inspired by gull wings; *ii*) a kinematical model to describe the process of wing adaptation based on one mechanism observed in the flight of gulls (folding-wing approach); and *iii*) a version of the unsteady vortex-lattice methods (UVLM) that allows taking nonlinear and unsteady aerodynamic phenomena into account. The model was specially developed to study the aerodynamic behavior during wing adaptation. A simulation for a twisting-flapping wing was performed in order to validate the numerical model. The present results are in close agreement with those obtained in previous studies based on the Euler equations, but required much less execution time. The numerical simulations of a bioinspired morphing wing showed the strong dependence between the prescribed kinematics and the aerodynamic characteristics, which evidences the importance of studying the process of wing adaptation. UVLM is shown to be ideal for preliminary analysis of bioinspired morphing wings.

1. INTRODUCTION

A developing technology based on morphing wings is the basis for a new generation of Unmanned Aerial Vehicles (UAVs) that will be capable of a variety of extraordinary maneuvers by reconfiguring its wings during flight as birds do. During a single mission, a morphing wing can adapt to improve maneuverability when needed and to reduce fuel consumption at other times. These UAVs, called Morphing Aircraft, could be significantly more efficient than today's conventional UAVs and lower the overall operational costs of multi-task missions.

The literature offers a classification [1, 2] of morphing concepts according to the method used to change the wing's shape. These methods include changing camber [3, 4], twist [5], sweep [6], and span [7, 8]. One of the first applications of variable-geometry wings, the *Swing Wing*, was implemented in the Bell-X5 in 1951. The aim was to provide a high lift-drag ratio in the unswept position for low-speed takeoff and landing and reduced drag at high-speed cruise in the sweptback position. This concept has been successfully applied in several military aircraft such as the General Dynamics F-111 Aardvark (1964) and the Grumman F-14 Tomcat (1970), among others [9].

Several research programs related to morphing technology have been conducted since 1979 [10]. Between 1995 and 2001, the US Defense Advanced Research Projects Agency (DARPA) and other organizations conducted the Smart Wing Program (SWP). Its main goal was to develop control surfaces by using smart materials that could rapidly change the aerodynamic and aeroelastic characteristics in flight for military aircraft [11]. In 2002, as an extension of the activities developed in the SWP, DARPA started a program called Morphing Aircraft Structures (MAS) aiming to design and build variable-geometry wing structures able to substantially change a wing's shape and area [12]. As part of the MAS

program, Lockheed Martin developed a morphing concept that allows significant changes to be made through a folding mechanism, as observed in birds, where the span, aspect ratio and effective sweep angle can experience significant changes. According to this concept, the wing can adapt to a range of flight conditions from a low-speed loiter to a high-speed dash [13, 14]. On the other hand, researchers at the University of Florida have developed and built a series of micro air vehicles (MAVs) to explore the flight dynamics [15] and characteristics of the morphing gull-wing concepts that use a folding-wing approach [16].

Despite the technological advances made in recent years, there are still many uncertainties related to the design of a functional UAV based on the concept of morphing wings. One is the aerodynamic aspect, which is currently poorly understood. Prediction of aerodynamic loads is necessary in order to perform different analyses, such as to evaluate the energy requirements to change the wing's shape [17] and, while the wing is morphing, to explore the flight dynamics [18], to predict the aeroelastic response [19], and to analyze the stress state in the wing's structure [20], among others. Several techniques have been used to compute the aerodynamic loads, such as Prandtl's lifting-line theory [21, 22], classical panel methods [23] and the vortex-lattice method for steady flows [24]. Computational tools based on computational fluid dynamics (CFD) have also been developed [20, 25]; however, most of them implement steady-flow models.

Of interest here are morphing-wing concepts that involve rapid changes, a capability necessary to achieve high maneuverability; thus modeling unsteady phenomena is very important. UVLM are appealing because of their low computational costs, use of inherent free-wake models to capture unsteady aerodynamic interference among various components, and rather good accuracy. The pioneering works in the development of UVLM were carried out by Belotserkovskii [26] and researchers at Virginia Tech [27, 28]. Perhaps, the most comprehensive description of UVLM was given by Katz and Plotkin [29].

Obradovic and Subbarao [18] implemented a version of UVLM to study the flight dynamics of a morphing-aircraft model; however, because the morphing speed is slow compared with the forward velocity of the aircraft, an unsteady model of the wake was not used. Jung and Kim [30] incorporated an unsteady wake model in order to study the aerodynamic behavior of a folding-wing concept developed by Lockheed Martin. Their numerical results show that the effect of a large folding angular velocity is an important factor that cannot be ignored. More recently, Wang and Zhang [31] also used UVLM to study the unsteady aerodynamics of a morphing wing that changes its dihedral angle with constant angular velocity. Their results demonstrate that the method is capable of accurately predicting many of the features that characterize complex morphing-wings flight.

In this paper, we present a numerical model that can be used to study the nonlinear and unsteady aerodynamic behavior of morphing wings inspired by the flight of birds. To change the wing shape we use a folding-wing mechanism. The model includes: *i*) a wing topology inspired by gull wings, whose geometric data are extracted from the literature; *ii*) a kinematical model to describe the process of wing adaptation based on a mechanism observed in the flight of gulls and other birds; and *iii*) a version of UVLM that allows one to accurately account for the nonlinear and unsteady aerodynamic phenomena involved. The present numerical model allows one to predict *i*) the flowfield around the wing's structure; *ii*) the position and shape of, as well as the distribution of vorticity in, the wakes shed from the sharp edges of the wings; and *iii*) the unsteady aerodynamic loads acting on the lifting surfaces.

To the best of the authors' knowledge, a nonlinear and unsteady aerodynamic study of gull-wings during the morphing process by means of a numerical model like the one mentioned above is not available in the literature, and it is the focus of the present work.

2. BIOINSPIRATION

The use of mechanisms inspired by the flight of birds is, perhaps, the key to developing aircraft with high flight capabilities. Recent discoveries in bird-flight mechanics and new insights for bioinspiration led many researches to consider birds as models for new generations of aircraft. Birds can change the shape of their wings and tails to improve maneuverability and performance under different flight conditions.

Gulls have been a biological source of inspiration [16] due to some of their range of flight characteristics such as slow low-level flying, fast steep dives, soaring at relatively high altitudes, and rapid take-offs. These flight capabilities are also desirable for small UAVs and could be obtained by using a morphing technology inspired by bird wings. Gulls use a variety of morphing techniques to

accomplish stabilization and high maneuverability. One of these techniques can be observed in Figure 1 which shows a gull reconfiguring its wings while in flight.

Figure 1: a) the wings are fully extended; b) and c) the wing sections are folded with different dihedral angles (http://www.jeffpippen.com/).

3. MODEL DESCRIPTION

In this section we develop a numerical model to study the aerodynamic characteristics of bioinspired, morphing-wing concepts. The model's geometry preserves certain morphological parameters of gull wings, and a folding mechanism is used to change the wing's shape, which is typical of gulls.

The geometric aspects associated with the wings are described in Section A, the kinematic model of the morphing process is described in Section B, and finally, the aerodynamic model is described in Section C.

3.1 Gull wing model

The morphing gull-wing model adopted in this paper corresponds to a herring gull (*Larus Argentatus*). Some basic data, such as the wing's span (b) and area (S) [32], summarized in Table 1, were maintained in the model. It consists of the right and the left wings, which are joined at the wing root. Because the two parts are mirror images, the model is developed only for the right wing (Figure 2*b*).

Table 1. Gull wing's data

Parameter	*Value*	*Source*
Wing span (b)	1.34 m	from ref [32]
Wing area (S)	0.197 m^2	from ref [32]
Wing mean chord (c_m)	0.147 m	computed (S/b)
Wing root chord (c_r)	0.177 m	chosen according [32]

Although the planform area of the wing is variable due to the morphing process, the wing area (S) is treated as a constant in the model to compute the aerodynamic coefficients. Thus, the absolute lift (L) and absolute induced drag (D_i) are directly proportional to the lift coefficient (C_L) and induced drag coefficient (C_{Di}) respectively.

To define the model geometry, we use an orthogonal Cartesian coordinate system (x, y, z). First, the leading and trailing edges, contained in the xy-plane ($z = 0$), are generated by using the data (x_{le}, y_{le}) and (x_{te}, y_{te}) shown in Figure 2*b*. These data are interpolated by using a cubic spline with not-a-knot conditions to obtain the expressions for the leading-edge $x = LE(y)$, and for the trailing edge $x = TE(y)$. Then the local chord is computed by

$$c = LE\left(y\right) - TE\left(y\right) \tag{1}$$

To complete the model, a seagull wing profile experimentally obtained by Liu *et al*. [33] is used. This profile can be generated from the camber and thickness distribution. However, in this work, the wing is aerodynamically modeled as a surface without thickness and therefore only the camber line is

considered, which is described by the following equations,

$$\frac{z}{c} = -\frac{z_m}{c}\lambda(1-\lambda)\sum_{m=1}^{3} S_m (1-2\lambda)^{m-1}; \quad \frac{z_m}{c} = \frac{0.14}{1+1.333\xi^{1.4}}; \quad \xi = \frac{2y}{b}; \quad \lambda = \frac{x-TE}{c} \tag{2}$$

where z_m is the local maximum camber of the profile. The values of the coefficients are S_1=3.874, S_2 = -0.807 and S_3 = 0.771; and the dimensionless variables λ and ξ are between 0 and 1.

An actual gull wing and the computational model are shown in Figure 2. Each wing is represented by two parts: the inner wing and the outer wing. In Figure 2*b*, the boundary between these parts and the geometric aspects of the wing are pointed out.

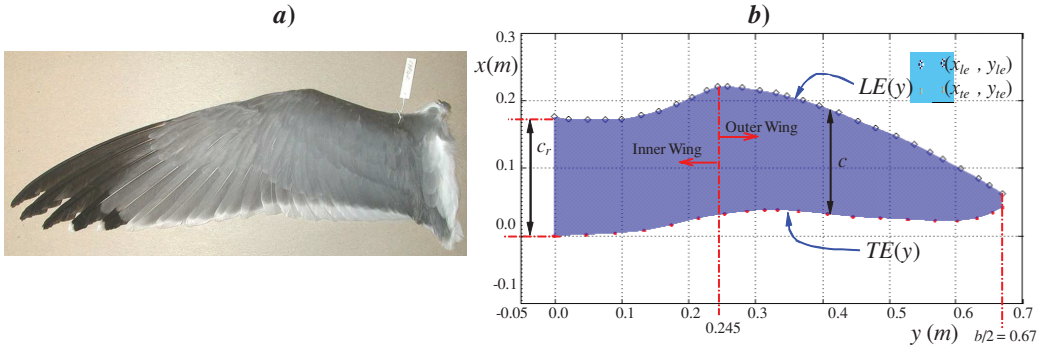

Figure 2: a) real gull wing (http://seanetters.wordpress.com). b) geometry of the bioinspired wing.

3.2 Kinematic Model

In this section, a description of the kinematic model used to compute the position and the velocity of an arbitrary point on the wing is presented. Since the motion of the wing is symmetric with respect to the *xz*-plane, only the kinematic description for the right wing is presented.

It is necessary to consider the camber line in the wing root (center line), which is the intersection between the left and right wings. This line, contained in the plane of symmetry *xz*, is important because in the morphing process the wing parts rotate around it. The center line does not move during the morphing process.

The inner and outer parts of the wing are connected and can move with respect to each other. The folding motion of the inner wing can be described by the dihedral angle θ_B and that of the outer wing by the dihedral angle θ_C (see Figure 3). The difference between θ_C and θ_B, denoted by θ_{BC}, is used to facilitate the mathematical description.

In order to model different time variations of the dihedral angles, we use the following expressions:

$$\theta_B(t) = \begin{cases} 0 & 0 \le t \le T_I \\ \theta_B^S\left(\dfrac{t-T_I}{(T_S-T_I)} - \dfrac{1}{2\pi}sin\left(\dfrac{2\pi}{T_S-T_I}(t-T_I)\right)\right) & T_I < t \le T_S \\ \theta_B^S & T_S < t \le T_F \end{cases}$$

$$\theta_C(t) = \begin{cases} 0 & 0 \le t \le T_I \\ \theta_C^S\left(\dfrac{t-T_I}{(T_S-T_I)} - \dfrac{1}{2\pi}sin\left(\dfrac{2\pi}{T_S-T_I}(t-T_I)\right)\right) & T_I < t \le T_S \\ \theta_C^S & T_S < t \le T_F \end{cases} \tag{3}$$

From these equations, it follows that the wing remains fully extended until time T_I; and then the morphing process begins by varying the dihedral angles until time T_S, where the wing takes a configuration which is maintained in a steady state and is determined by the angles θ_B^S and θ_C^S. The simulation ends at T_F.

3.2.1 Reference systems and transformation of coordinates

Four reference frames are used here: *i*) the first system is fixed to the center line $\mathbf{A} = (\mathbf{a}_1, \mathbf{a}_2, \mathbf{a}_3)$, which is associated with the coordinate axes (x, y, z) previously defined (it is important to note that the geometry of the entire wing is generated in this system); *ii*) the second system is fixed to the inner wing $\mathbf{B} = (\mathbf{b}_1, \mathbf{b}_2, \mathbf{b}_3)$; *iii*) the third one is fixed to the outer wing $\mathbf{C} = (\mathbf{c}_1, \mathbf{c}_2, \mathbf{c}_3)$; and *iv*) an inertial or Newtonian system $\mathbf{N} = (\mathbf{n}_1, \mathbf{n}_2, \mathbf{n}_3)$. The unit vectors $\mathbf{a}_i$, $\mathbf{b}_i$, $\mathbf{c}_i$ and $\mathbf{n}_i$ form right-handed orthonormal bases [34] associated with **A**, **B**, **C** and **N**, respectively. The origin of system **B** is located on plane xz, and the vector $\mathbf{b}_1$ coincides with $\mathbf{a}_1$. The origin of system **C** is on the intersection between the inner and the outer wing, and the vector $\mathbf{c}_1$ is parallel to $\mathbf{b}_1$.

The inertial system **N** is oriented such that $\mathbf{n}_1$ and $\mathbf{n}_2$ lie in a horizontal plane with $\mathbf{n}_1$ pointing in the direction of flight (or equivalently opposite the direction of the free stream) and $\mathbf{n}_3$ pointing downward. The orientation of system **A** with respect to the inertial system **N** consists of a 1-rotation of system **A** around $\mathbf{n}_2$ through the angle of attack α. The orientation of system **B** with respect to system **A** consists of a 1-rotation of system **B** around $\mathbf{a}_1$ through the angle θ_B. The orientation of system **C** with respect to **B** consists of a 1-rotation of system **C** around an axis parallel to $\mathbf{b}_1$ through the angle θ_{BC},

The coordinate transformation from system **A** to system **N** can be achieved using the rotation matrix $[\mathbf{T}_{\mathrm{NA}}]$; the transformation from the system **B** to **A** can be achieved using the rotation matrix $[\mathbf{T}_{\mathrm{AB}}]$, and the transformation from system **C** to **B** can be achieved using the rotation matrix $[\mathbf{T}_{\mathrm{BC}}]$. All these rotation matrices are given in equation (4):

$$\left[\mathbf{T}_{\mathrm{NA}}\right]=\begin{bmatrix} \cos\alpha & 0 & \sin\alpha \\ 0 & 1 & 0 \\ -\sin\alpha & 0 & \cos\alpha \end{bmatrix};\left[\mathbf{T}_{\mathrm{AB}}\right]=\begin{bmatrix} 1 & 0 & 0 \\ 0 & \cos\theta_B & -\sin\theta_B \\ 0 & \sin\theta_B & \cos\theta_B \end{bmatrix};\left[\mathbf{T}_{\mathrm{BC}}\right]=\begin{bmatrix} 1 & 0 & 0 \\ 0 & \cos\theta_{BC} & -\sin\theta_{BC} \\ 0 & \sin\theta_{BC} & \cos\theta_{BC} \end{bmatrix} \quad (4)$$

The transformations of coordinates from systems **B** and **C** to system **N** are achieved by the rotation matrices $[\mathbf{T}_{\mathrm{NB}}]$ and $[\mathbf{T}_{\mathrm{NC}}]$, respectively:

$$\left[\mathbf{T}_{\mathrm{NB}}\right]=\left[\mathbf{T}_{\mathrm{NA}}\right]\left[\mathbf{T}_{\mathrm{AB}}\right] \qquad \left[\mathbf{T}_{\mathrm{NC}}\right]=\left[\mathbf{T}_{\mathrm{NA}}\right]\left[\mathbf{T}_{\mathrm{AB}}\right]\left[\mathbf{T}_{\mathrm{BC}}\right] \quad (5)$$

3.2.2 Position and velocity of an arbitrary point on the wing

The position vector of an arbitrary point p located on the outer wing with respect to system **N** is given by,

$$\mathbf{R}_p = \mathbf{R}_{\mathrm{NA}} + \mathbf{R}_{\mathrm{AB}} + \mathbf{R}_{\mathrm{BC}} + \mathbf{r}_p \quad (6)$$

where, $\mathbf{R}_{\mathrm{NA}}$ is the position vector of the origin of system **A**, with respect to system **N**; $\mathbf{R}_{\mathrm{AB}}$ is the position vector of the origin of system **B**, with respect to system **A**; $\mathbf{R}_{\mathrm{BC}}$ is the position vector of the origin of system **C**, with respect to system **B**; and $\mathbf{r}_p$ is the position vector of point p with respect to system **C**. Then, $\mathbf{R}_p$ can be formulated in system **N** by,

$$\left\{\mathbf{R}_p\right\}_N = \left\{\mathbf{R}_{\mathrm{NA}}\right\}_N + \left[\mathbf{T}_{\mathrm{NA}}\right]\left\{\mathbf{R}_{\mathrm{AB}}\right\}_A + \left[\mathbf{T}_{\mathrm{NB}}\right]\left\{\mathbf{R}_{\mathrm{BC}}\right\}_B + \left[\mathbf{T}_{NC}\right]\left\{\mathbf{r}_p\right\}_C \quad (7)$$

where, sub-indices N, A, B and C indicate that a vector is expressed in systems **N**, **A**, **B**, and **C**, respectively.

The velocity vector of point p is obtained by taking the total time derivative of position vector $\mathbf{R}_p$ performed by an observer in system **N**.

$$ {}^{N}\mathbf{V}_{p} = \frac{{}^{N}d}{dt}\mathbf{R}_{\mathrm{NA}} + \frac{{}^{N}d}{dt}\mathbf{R}_{\mathrm{AB}} + \frac{{}^{N}d}{dt}\mathbf{R}_{\mathrm{BC}} + \frac{{}^{N}d}{dt}\mathbf{r}_{p} \tag{8} $$

The total time derivatives shown in equation (8) are computed by means of the transport theorem [35]:

$$ \begin{aligned} \frac{{}^{N}d}{dt}\mathbf{R}_{\mathrm{AB}} &= \frac{{}^{A}d}{dt}\mathbf{R}_{\mathrm{AB}} + {}^{N}\boldsymbol{\omega}^{A}\times\mathbf{R}_{\mathrm{AB}} \\ \frac{{}^{N}d}{dt}\mathbf{R}_{\mathrm{BC}} &= \frac{{}^{B}d}{dt}\mathbf{R}_{\mathrm{BC}} + {}^{N}\boldsymbol{\omega}^{B}\times\mathbf{R}_{\mathrm{BC}} \\ \frac{{}^{N}d}{dt}\mathbf{r}_{p} &= \frac{{}^{C}d}{dt}\mathbf{r}_{p} + {}^{N}\boldsymbol{\omega}^{C}\times\mathbf{r}_{p} \end{aligned} \tag{9} $$

where ${}^{N}\boldsymbol{\omega}^{A}$, ${}^{N}\boldsymbol{\omega}^{B}$ and ${}^{N}\boldsymbol{\omega}^{C}$ are the angular velocity of system **A** with respect to system **N**, the angular velocity of system **B** with respect to **N**, and the angular velocity of system **C** with respect to **N**, respectively, which can be computed as follows:

$$ \begin{aligned} &{}^{N}\boldsymbol{\omega}^{B} = {}^{N}\boldsymbol{\omega}^{A} + {}^{A}\boldsymbol{\omega}^{B}; \quad {}^{N}\boldsymbol{\omega}^{C} = {}^{N}\boldsymbol{\omega}^{A} + {}^{A}\boldsymbol{\omega}^{B} + {}^{B}\boldsymbol{\omega}^{C} \\ &{}^{N}\boldsymbol{\omega}^{A} = \dot{\alpha}\,\mathbf{a}_{2}; \quad {}^{A}\boldsymbol{\omega}^{B} = \dot{\theta}_{B}\,\mathbf{b}_{1}; \quad {}^{B}\boldsymbol{\omega}^{C} = \dot{\theta}_{BC}\,\mathbf{c}_{1} \end{aligned} \tag{10} $$

where the dot notation is used to indicate time derivatives.

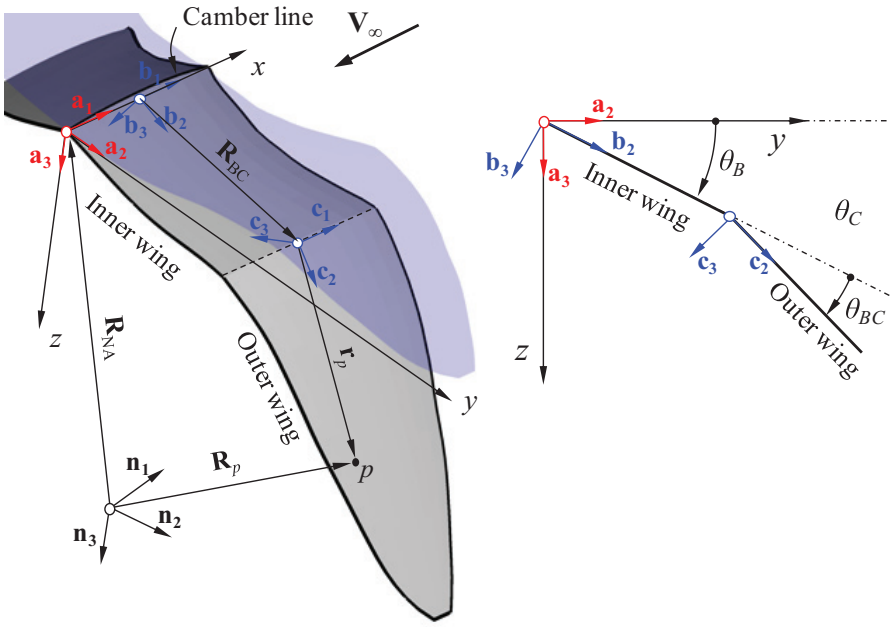

Figure 3: dihedral angles, reference systems and position vector of a generic point p on the wing.

Since the vectors $\mathbf{R}_{\mathrm{AB}}$, $\mathbf{R}_{\mathrm{BC}}$ and $\mathbf{r}_p$ are fixed to **A**, **B** and **C** frames, respectively, their time derivatives with respect to these systems are zero. Furthermore, if the angle of attack α does not vary in time, then ${}^{N}\boldsymbol{\omega}^{A} = \mathbf{0}$. With all this, the velocity of p in the inertial frame **N** becomes,

$$ {}^{N}\mathbf{V}_{p} = {}^{N}\mathbf{V}_{A} + {}^{N}\boldsymbol{\omega}^{B}\times\mathbf{R}_{\mathrm{BC}} + {}^{N}\boldsymbol{\omega}^{C}\times\mathbf{r}_{p} \tag{11} $$

where, ${}^{N}\mathbf{V}_{A}$ is the velocity of the system **A** origin with respect to system **N** (i.e. the time derivative of $\mathbf{R}_{\mathrm{NA}}$). Then the velocity can be expressed in the system **N** by equation (12):

$$\left\{ {}^{N}\mathbf{V}_{p} \right\}_{N} = \left\{ {}^{N}\mathbf{V}_{A} \right\}_{N} + \left[\mathbf{T}_{\mathrm{NB}} \right] \left(\left\{ {}^{N}\boldsymbol{\omega}^{B} \right\}_{B} \times \left\{ \mathbf{R}_{\mathrm{BC}} \right\}_{B} \right) + \left[\mathbf{T}_{\mathrm{NC}} \right] \left(\left\{ {}^{N}\boldsymbol{\omega}^{C} \right\}_{C} \times \left\{ \mathbf{r}_{p} \right\}_{C} \right) \tag{12}$$

Equations (7) and (12) are only valid for the outer wing. The expressions for the position and velocity of an arbitrary point located on the inner wing can be obtained in the similar way.

3.3 Aerodynamic Model

3.3.1 General aspects

In this paper, UVLM is used to compute the aerodynamic loads acting on morphing wings. This method can be applied to lifting surfaces of any planform, camber, or twist. The lifting surface may undergo any time-dependent deformation, and execute any maneuver in moving air. The flow surrounding the lifting surface is assumed to be inviscid, incompressible, and irrotational over the entire flowfield, excluding the solid boundaries and the wakes.

Due to the relative motion between the wing and the fluid and viscous effects, vorticity is generated in the fluid in a thin region next to the wing's surface (the boundary layer). The boundary layers on the upper and lower surface are merged into a single vortex sheet. Vorticity in this sheet is shed from the sharp edges (trailing edge and wing tips) in order for the pressures in the merging flows coming off the upper and lower sides of the lifting surfaces to be the same. The shed vorticity forms the wake as it moves down stream with the fluid particles in order for the pressure in the flow downstream to be continuous and the wake to be force-free.

The calculation of the velocity field associated with the vorticity is expedited by replacing the continuous vortex sheet with a lattice of discrete vortex lines. The boundary layers are represented by bound-vortex lattices (they are attached or bound to the lifting surface and move with it) and the wakes are represented by free-vortex lattices (they move freely with the flow so that their position and the distribution of vorticity in them are determined as part of the solution). The bound- and free-vortex lattices are joined along the sharp edges where shedding occurs, the same edges at which the Kutta condition is imposed in a steady flow. A detailed description of UVLM can be found in [36, 37].

3.3.2 The Mathematical problem

The velocity field for the fluid particles is a function of position **R** and time *t*, is denoted by $\mathbf{V}(\mathbf{R};t)$, and satisfies the continuity equation for an incompressible flow:

$$\nabla \cdot \mathbf{V}\left(\mathbf{R};t\right) = 0 \tag{13}$$

Because the flow is irrotational outside the boundary layers and the wakes, the velocity field may be expressed as the gradient of a velocity potential function, $\Phi(\mathbf{R}, t)$:

$$\mathbf{V}\left(\mathbf{R};t\right) = \nabla\Phi\left(\mathbf{R};t\right) \tag{14}$$

By substituting equation (14) into equation (13), one obtains the expression that governs the potential function:

$$\nabla^{2}\Phi\left(\mathbf{R};t\right) = 0 \tag{15}$$

A set of boundary conditions (BCs) must be added to this equation. The first BC, commonly called "the no-penetration boundary condition", requires the normal component of the velocity of the fluid relative to the solid surface to be zero at the surface boundaries. This BC can be mathematically stated as,

$$\left(\mathbf{V} - \mathbf{V}_{S}\right) \cdot \mathbf{n}\Big|_{S} = \left(\nabla\Phi - \mathbf{V}_{S}\right) \cdot \mathbf{n}\Big|_{S} = 0 \tag{16}$$

where $\mathbf{V}_S$ is the velocity of, and $\mathbf{n}$ is a vector normal to, the lifting surface. In general, both $\mathbf{V}_S$ and $\mathbf{n}$ vary in space and time.

The second BC, called "the regularity condition", requires the disturbances due to the wing's motion to die out far from it and its wake. This condition can be stated as,

$$\lim_{\mathbf{R}\to\infty}\left\|\nabla\Phi\right\|_2 = \left\|\mathbf{V}_\infty\right\|_2 \tag{17}$$

where, $\mathbf{V}_\infty$ is the free-stream velocity. The disturbance velocity is computed according to the Biot-Savart law, and hence, the BC given by equation (17) is satisfied identically. For incompressible potential flow, the velocity is obtained independent of pressure by solving the continuity equation. Once the velocity field is known, the pressure field is calculated using the unsteady version of Bernoulli's equation. In addition to the two BCs stated above, the Kelvin-Helmholtz theorem and the unsteady Kutta condition are used to determine the strength and position of the free-vortex sheets (the wakes).

The integral representation of the velocity field $\mathbf{V}$ is given by equation (18):

$$\mathbf{V}\left(\mathbf{R},t\right) = \frac{1}{4\pi}\iiint_V \frac{\boldsymbol{\Omega}\left(\mathbf{R},t\right)\times\left(\mathbf{R}-\mathbf{R}_0\right)}{\left\|\mathbf{R}-\mathbf{R}_0\right\|_2^3}\,dV_0 \tag{18}$$

where, $\boldsymbol{\Omega} = \nabla \times \mathbf{V}$ is the vorticity field; $\mathbf{R}_0$ is a position vector on the region V_0 of the fluid domain. When all the vorticity is contained in a finite, straight-line segment, equation (18) becomes the Biot-Savart law:

$$\mathbf{V}\left(\mathbf{R},t\right) = \frac{\Gamma\left(t\right)}{4\pi}\frac{\mathbf{L}\times\mathbf{r}_1}{\left\|\mathbf{L}\times\mathbf{r}_1\right\|_2^2}\left[\mathbf{L}\cdot\left(\mathbf{e}_1-\mathbf{e}_2\right)\right] \tag{19}$$

where $\Gamma(t)$ is the spatially constant circulation around the vortex segment, $\mathbf{R}$ is the position vector of the point where the velocity is computed; $\mathbf{r}_1$ and $\mathbf{r}_2$ are the position vectors of this point relative to the ends of the vortex segment; $\mathbf{e}_1$ and $\mathbf{e}_2$ are the unit vectors parallel to $\mathbf{r}_1$ and $\mathbf{r}_2$, respectively; and $\mathbf{L} = \mathbf{r}_1 - \mathbf{r}_2$.

3.3.3 Unsteady vortex lattice method (UVLM)

In UVLM, the vortex sheets are replaced by lattices of short straight vortex segments of spatially constant circulation $\Gamma(t)$. These segments divide the wing's surface into a finite number, N_P, of typically nonplanar, quadrilateral elements of area with straight edges, which are often called panels. The model is completed by joining the free-vortex lattices (wakes) to the bound-vortex lattice along the edges where separation occurs. The location of separation is user-supplied and typically based on experience.

In order to reduce the size of the problem, each element is considered to be enclosed by a closed loop consisting of four vortex segments. Each quadrilateral element of the bound lattice has a single unknown circulation $G(t)$ associated with it instead of four unknown circulations around each of the short, vortex-line segments along its edges. Consequently, the requirement of spatial conservation of circulation is automatically satisfied throughout the lattices. The circulation $\Gamma(t)$ around a straight vortex segment along an edge of an element is determined by the circulations $G(t)$ of the vortex-rings that contain this segment.

Because the bound vortex sheet is approximated by a lattice with a finite number of elements (Figure 4) and, hence, a finite number of *G's*, the no–penetration condition given by equation (16) can be satisfied at only a finite number of points; the chosen points, called control points (CPs), are the centroids of the corner points of each panel (also called aerodynamic nodes). The no-penetration condition, equation (16), can be expressed in discrete form and in terms of the velocity:

$$\left(\mathbf{V}_B + \mathbf{V}_W + \mathbf{V}_\infty - \mathbf{V}_S\right)_i \cdot \hat{\mathbf{n}}_i = 0, \qquad i = 1,\ldots,N_P \tag{20}$$

where the fluid velocity evaluated at the control points is divided into three parts: $\mathbf{V}_B$ is associated with

the bound-vortex lattice, $\mathbf{V}_W$ with the free-vortex lattice (the wake), and $\mathbf{V}_\infty$ with the free-stream; $\mathbf{V}_S$ is the velocity of the lifting surface at the control point, $\hat{\mathbf{n}}_i$ is the cross product of the diagonal vectors of element i, and N_p is the number of panels (elements). The no-penetration condition is now expressed as N_p algebraic equations.

The next step is to use equation (19) to set up an influence matrix, A_{ij}, such that at the control point of panel i, $\mathbf{V}_B \cdot \mathbf{n}_i = \Sigma\, A_{ij}(t)G_j(t)$. Substituting this expression into equation (20) yields the system of algebraic equations for the $G_j(t)$ that must be solved at each time step:

$$\sum_{j=1}^{N_P} A_{ij}(t)\, G_j\left(t\right) = -\left(\mathbf{V}_\infty + \mathbf{V}_W - \mathbf{V}_S\right)\cdot \hat{\mathbf{n}}_i, \qquad i = 1, \ldots, N_P \tag{21}$$

The wing does not move forward, instead an air stream flows past it.

At the end of each time step, in order to satisfy the unsteady Kutta condition, the quadrilateral vortex rings around the elements along the trailing edge and at the wing tip are shed into the flowfield. They remain attached in the same order as they were on the wing's surface and become part of the grids that approximate the free-vortex sheets. Each vortex ring is convected downstream with the flow while the G associated with it remains constant, and thereby the vorticity distribution in and the shape of the wake are determined as part of the solution. To convect the vortex ring, the ends of the discrete straight vortex segments in the ring are moved at the local particle velocity $\mathbf{V}$ to new positions, denoted $\mathbf{R}(t + \Delta t)$, according to the following:

$$\mathbf{R}\left(t+\Delta t\right) = \mathbf{R}\left(t\right) + \mathbf{V}(\mathbf{R},t)\,\Delta t \tag{22}$$

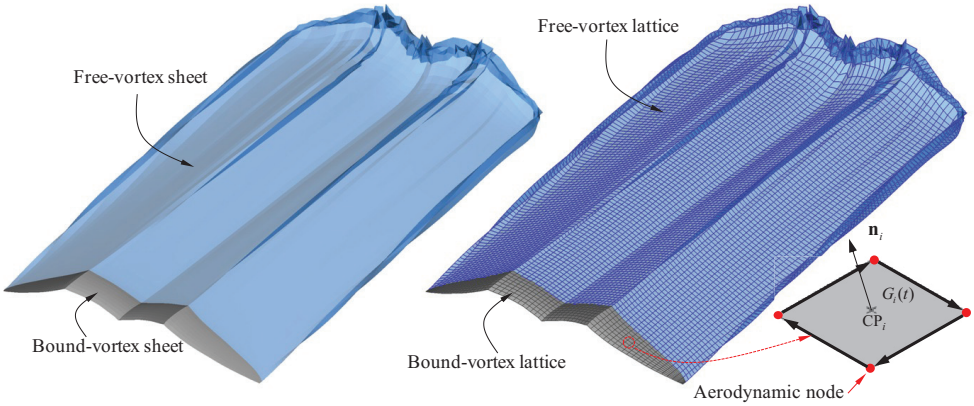

Figure 4: vortex sheets and a typical panel.

In Figure 4, the solution of a numerical experiment showing the development of the wake after 200 time steps is given. This case corresponds to an impulsive start, *i.e.* the fluid surrounding the wing is at rest and then suddenly starts moving with a uniform and constant velocity $\mathbf{V}_\infty$.

3.3.4 Computation of Aerodynamic Loads

The force on each area element in the bound lattice is calculated by determining the pressure jump across the lifting surface at the control point and then multiplying it by the area of the element and the unit vector normal to the element. The total force is then calculated by a vector sum. The pressure jump is calculated from a version of Bernoulli's equation for unsteady flows which is given by equation.

$$\frac{\partial}{\partial t}\Phi(\mathbf{R},t) + \frac{1}{2}\mathbf{V}(\mathbf{R},t)\cdot\mathbf{V}(\mathbf{R},t) + \frac{p(\mathbf{R},t)}{\rho} = \frac{1}{2}\mathbf{V}_\infty\cdot\mathbf{V}_\infty + \frac{p_\infty}{\rho} \tag{23}$$

where ρ is the fluid density, p is the pressure, and p_∞ is the free-stream pressure. The details of this equation and the development to obtain the pressure jump are found in [36, 37].

4. NUMERICAL RESULTS

In this section, some results obtained using the present numerical model are presented. The code was written in FORTRAN 90 and compiled to run on Linux platforms. Automatic optimization options have been used to achieve high performance. For all cases shown in this paper, the code was run on a desktop computer with a processor Intel(R) Core(TM) i7 950 (Clock Speed 3.07GHz, number of Cores 4, number of Threads 8, 8MB Cache memory) and a RAM DDR3 of 4GB.

First, a numerical simulation for a flapping-twisting wing was developed in order to verify the present model by comparing the present results with those obtained in previous studies from the Euler equations [38]. Then, a mesh sensitivity analysis was developed in order to determine a suitable mesh for the numerical simulations of flows over gull wings. Finally, a set of numerical simulations is presented with the purpose of understanding the aerodynamic behavior of the morphing gull-wing concept during the morphing process.

4.1 Verification of the Numerical Model

To verify the present numerical model, we compare the results obtained with the present simulation of a rectangular flapping-twisting wing to those obtained previously by Neef and Hummel [38] with the Euler equations for $M = 0.3$. They considered a rectangular wing with an aspect ratio $AR = 8$, a NACA 0012 airfoil profile.

There is a sinusoidal flapping rotation of the leading edge about the root cord with an amplitude of 15 degrees and a reduced frequency of $k = 0.1$ ($k \equiv \omega c/2V_\infty$, where ω is the flapping frequency and c is the wing's chord).

In addition to the flapping motion about the root cord, there is a sinusoidal twisting rotation about the leading edge. The amplitude of the twisting motion varies linearly along the semi-span with a maximum rotation of 4 degrees at the tip.

The root chord, the leading edge and the chordwise cross sections remain straight during the motion. Both the flapping and the twisting motions have the same frequency, but they are not in phase. The twisting motion renders the elements non-planar, which is not problematic for UVLM.

The kinematic model developed for morphing wings was easily modified to describe the flapping-twisting motion of Neef's and Hummel's wing. The systems **B** and **C** were located at the leading edge, and the rotation matrix $[\mathbf{T}_{BC}]$ was the following:

$$\left[\mathbf{T}_{BC}\right] = \begin{bmatrix} \cos\beta & 0 & -\sin\beta \\ 0 & 1 & 0 \\ \sin\beta & 0 & \cos\beta \end{bmatrix}$$

The angle β determines the orientation of system **C** with respect to system **B**; it is associated with the twisting motion. The location of the origin of the system **C** along the span is determined by a ζ, a function of position along the span; see (Figure 5) which shows the location of the references systems. The angles that describe the motion of the wing are expressed as follows:

$$\theta_B = \left(\frac{15\pi}{180}\right)\cos(\omega t) \qquad \beta = -\left(\frac{4\pi}{180}\right)\left(\frac{2\zeta}{b}\right)\sin(\omega t)$$

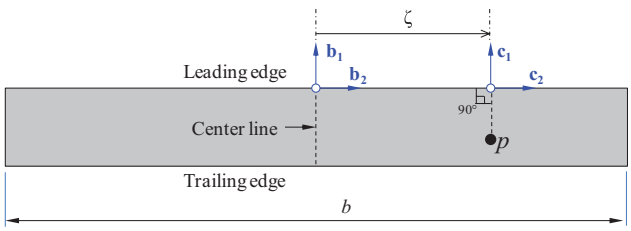

Figure 5: location of the reference systems on the flapping-twisting wing.

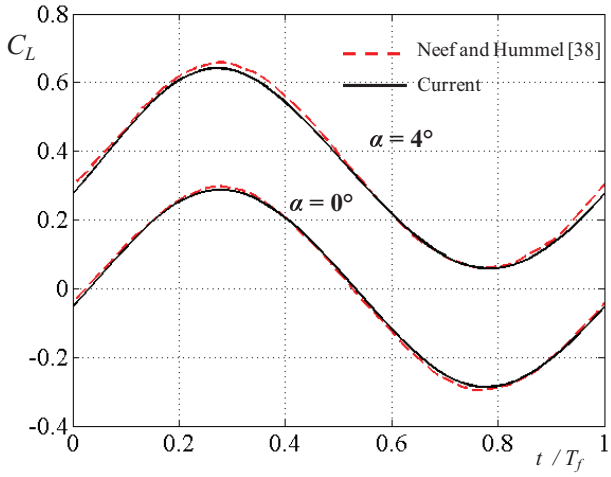

Figure 6: comparison of the present lift coefficient with results from [38].

Comparative results are shown in Figure 6 for a flapping-twisting wing with its root chord inclined at two constant angles of attack: 0 and 4 degrees. A mesh of 6 x 20 panels in the chordwise and spanwise directions, respectively, was used to obtain the present result. The agreement between the results given in [38] and those obtained with the numerical technique proposed here is very good in both cases. The present results were obtained with considerable speed and ease.

4.2 A mesh-sensitivity analysis

An analysis to select a suitable mesh to perform the numerical simulations is presented next. In this analysis a process of wing adaptation was simulated for different meshes m_i, and then a suitable mesh was chosen according to an established criterion. The gull-wing was reconfigured in time by prescribing the dihedral angles $\theta_B(t)$ and $\theta_C(t)$ given in equation (3). The values used in this analysis were:

$$\alpha = 5° \quad \theta_B^S = -30° \quad \theta_C^S = 0° \quad T_I = 25\frac{c_0}{V_\infty} \quad T_S = 60\frac{c_0}{V_\infty} \quad T_F = 70\frac{c_0}{V_\infty} \quad V_\infty = 12.4\left[\frac{m}{s}\right]$$

where the magnitude of the free-stream velocity, V_∞, was chosen according the cruise airspeed of gulls [32].

In the analysis seven meshes were utilized, and the details of the mesh density on half of the wing are given in Table 2. The numbers of panels in the chordwise (*NPCH*) and the spanwise (*NPSP*) directions were chosen in order to obtain a mesh with nearly square panels.

First, the lift coefficient, C_L, was obtained for every mesh and plotted in Figure 7. The results show that as the density of the mesh increases, the difference between the solutions narrows. Before the wings starts to morph, the biggest difference can be observed around t = 0.35 seconds; and once the wings start moving, the biggest difference occurs at approximately t = 0.62 seconds. Then, when the wings reach their steady-state configuration, the difference for all time is less than at t = 0.35 and t = 0.62; hence, we only computed the difference at t = 0.35 and t = 0.62.

Table 2. Mesh density

Mesh	*Panels*	*NPCH*	*NPSP*		*Total*
			Inner Wing	Outer Wing	
m_0	2	3	5	16	
m_1	4	6	10	64	
m_2	6	9	15	144	
m_3	8	12	20	256	
m_4	10	15	25	400	
m_5	12	18	30	576	
m_6	14	21	35	784	

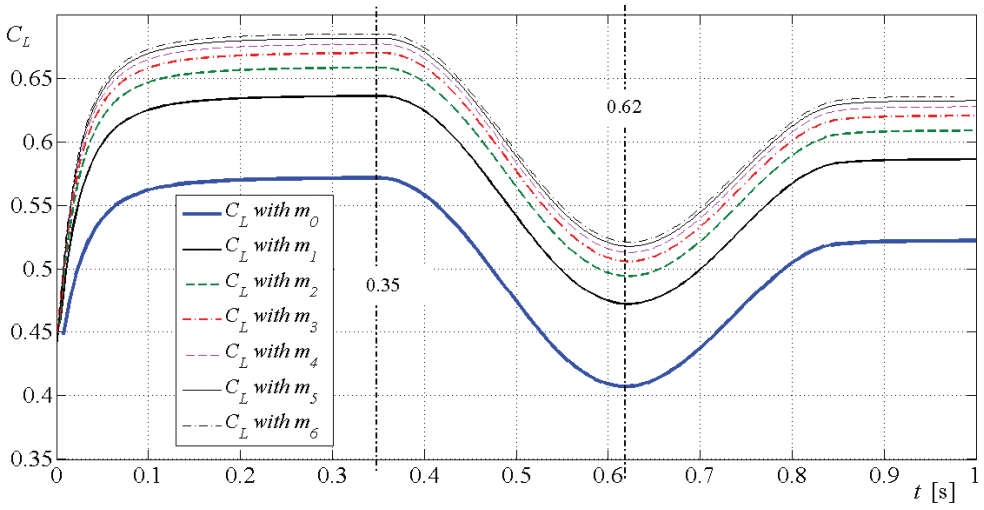

Figure 7: the lift coefficient for all meshes.

In order to establish a criterion for selecting a suitable mesh, the percentage difference between the lifts associated with meshes m_i and m_{i-1} is computed by equation (24):

$$d_i = \left| \frac{C_L \text{ with } m_i - C_L \text{ with } m_{i-1}}{C_L \text{ with } m_i} \right| \cdot 100 \tag{24}$$

A percentage difference of less than the 2% is considered acceptable.

Moreover, the time consumed, *tc*, or the computational cost to obtain the numerical solution is an important factor that was considered.

The percentage difference for $t = 0.35$ *s* and $t = 0.62$ *s* is shown in Figure 8*a*; and the time consumed for every mesh is plotted in Figure 8*b*. We note that d_i decreases asymptotically to zero and the difference at 0.62 *s* is bigger than the difference at 0.35 *s*; and on the other hand, *tc* experiences an exponential-like growth.

According to data presented in Figure 8, a suitable mesh is m_3; the difference between d_3 and d_4 is less than 1.3%, and the computational cost for m_3 (1.2 *hs*) is one-third of that for m_4 (3.6 *hs*). If a less dense mesh is chosen, for example m_2, its computational cost is lower but the accuracy is not acceptable. If a mesh with a higher density is chosen the accuracy increases; however it is not justified because of the large increase in computational cost.

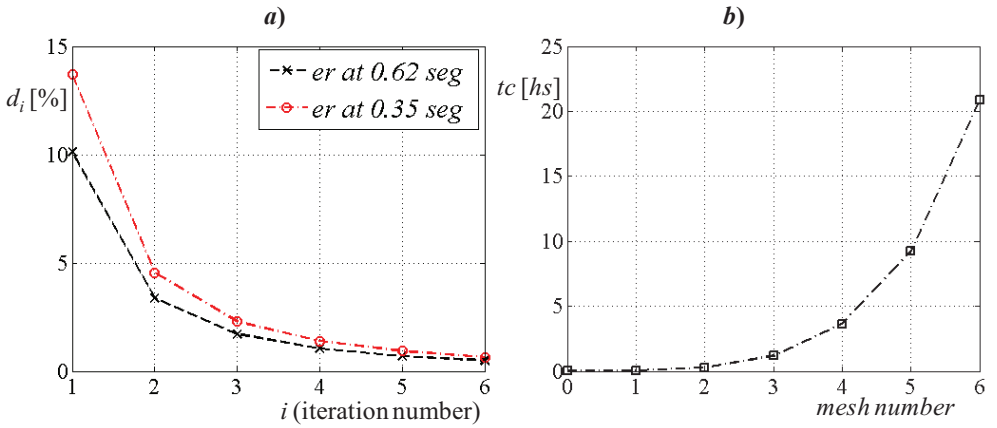

Figure 8: a) percentage difference. b) time consumed.

4.3 Numerical simulations of the morphing process

Three passages through the morphing processes were simulated with the mesh m_3 given in Table 2. The morphing wing was reconfigured in time by means of equation (3) with the values given in Table 3. In each case, two conditions were considered: (*i*) with shedding vorticity from the wing tips; and (*ii*) without shedding vorticity from the wing tips.

Table 3. Simulation data

Case	θ_B^S	θ_C^S	T_I	T_S	T_F	V_∞	α
I	-30°	30°	35 c_0/V_∞	70 c_0/V_∞	90 c_0/V_∞	12.4 [m/s]	5°
II	10°	30°					
III	-10°	-30°					

In Figure 9, the lift coefficients for the three cases are plotted as functions of time. There are only slight differences between the solutions obtained with conditions (*i*) and (*ii*); thus, the vorticity being shed from the wingtips may be ignored. For all three cases, the number of elements in the wake associated with the wingtips is 20% of the total in the wake; when the wing-tip elements are eliminated, the computational time is reduced by 35%.

During the first part of the flight simulation, when the wing is fully extended, the lift rapidly increases until the steady state is reached at T_I. During second part of the flight simulation $T_I<t<T_S$, which is the morphing process, the lift depends on the prescribed kinematics of the dihedral angles. In the third phase of the process after the morphing is completed, $t > T_S$, the wings approach new steady states.

In Case III, the lift smoothly decreases until it reaches a local minimum, $t \approx T_M$, and then it increases to a value that corresponds to the wing's configuration in the new steady state. In this case it appears that during the morphing process there could be a loss in altitude or perhaps a decrease in the rate of climb or an increase in the rate of descent.

In Case II, the lift increases during the morphing process to reach a local maximum, $t \approx T_M$, and then it begins to decrease until it reaches a value that corresponds to the wing's new configuration in the steady state. In this case it appears that the morphing process would produce a gain in altitude. With a little tweaking, the two morphing processes could lead to the same steady state both Case II and Case III, but the aircraft would be at different altitudes depending on the morphing process used.

In Case I, the lift behavior is different; it begins decreasing smoothly until the steady state solution is reached. The lift shows neither a local maximum nor a local minimum during the morphing.

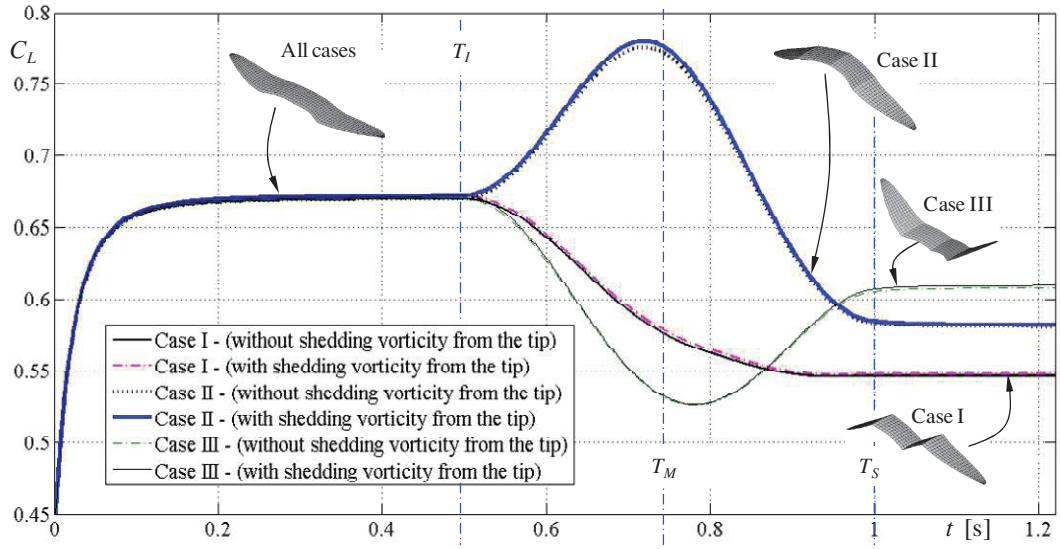

Figure 9: lift coefficient as a function of time

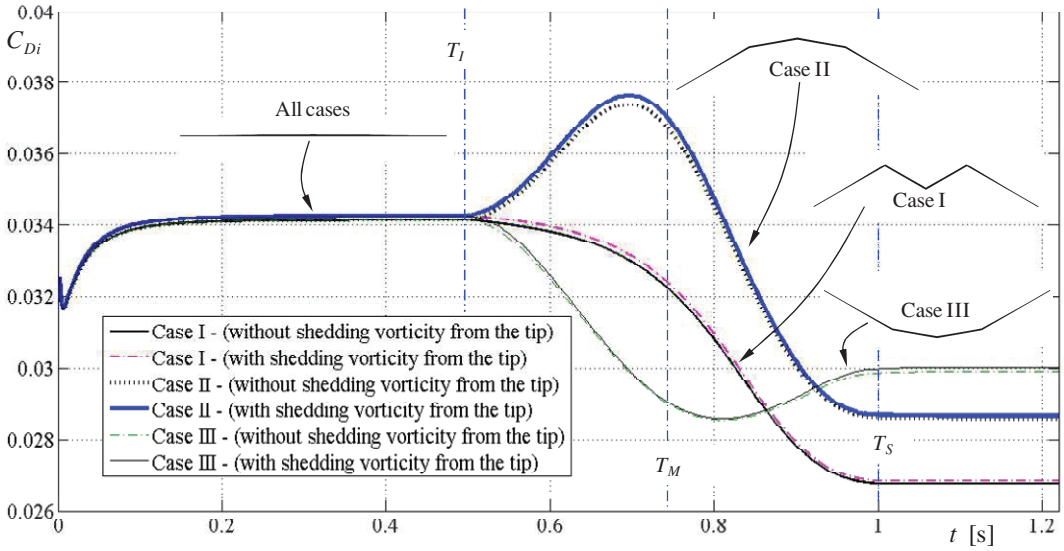

Figure 10: Induced drag coefficient as a function of time.

In Figure 10, the induced drag coefficients are plotted as functions of time for the three cases. Their behaviors are qualitatively similar though the values are much smaller. Again, the results obtained confirm that the vorticity shed from the wing tips does not have an important influence over the aerodynamic loads. Although the same expression, equation (3), was used for all three cases to morph the wings, both lift and drag exhibited different behaviors for different morphings due to the different combinations of θ_B^S and θ_C^S.

With some tweaking in the three cases, the wing could arrive at any (within reason) prescribed steady state lift, but most likely with the aircraft at different altitudes and different airspeeds (though the airspeed was held constant in these three example, it could be changed step-by-step).

The present model provides an accurate tool to account for 1) the strong dependence between the unsteady aerodynamic loads and the morphing motion and 2) the power needed to drive the morphing. All of which in turn constitutes an elegant tool for designing a morphing process that will efficiently take an aircraft from one steady state to another.

It is important to mention that the average weight of a typical gull is 11.4 N [32]; this is a reasonable weight for small UAVs. With this in mind, and considering a speed of 12.4 m/s, the necessary lift coefficient to maintain a bio-inspired vehicle aloft must be 0.6 or higher. Figure 9 shows that for Case III, in steady state, a value of the lift coefficient (C_L = 0.61) enough to keep the vehicle aloft is attained. However, the other two cases do not produce suitable values of lift for balancing the UAV weight.

Figure 11 shows the lift coefficient in steady state as function of the angle of attack for the three above-mentioned cases. These results show that for Case I and Case II it is necessary an angle of attack of 6° and 5.4° respectively to achieve the desired C_L.

The developed code automatically processes the data to generate movies that contribute to understanding the time variation of the pressure-jump distribution (ΔC_p) over the wings. In Figure 12, the pressure distribution for case II is shown at time T_I, $T_M = (T_I + T_S)/2$, and T_F. It is possible to locate the zones of maximum and minimum pressure jumps. At all times, the maximum ΔC_p occurs on the leading edge near the wingtips; at time T_M, when the wing is moving, this maximum value is near its highest. At all times, the minimum ΔC_p is located at the trailing edge near the wingtips. At the three instants, there is a gradual growth of ΔC_p from the trailing edge toward the leading edge. But this growth is not uniform along the span. It is not easy to see the chordwise variation of ΔC_p; thus in Figure 13 the pressure jump versus the dimensionless variable λ is plotted for the sections E, F and H which are indicated in Figure 12.

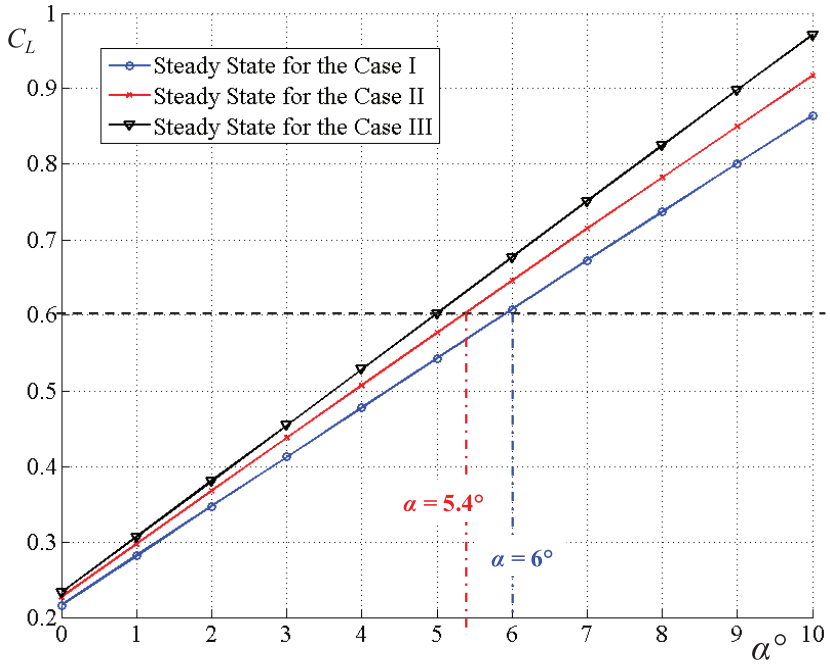

Figure 11: Lift coefficient versus angle of attack.

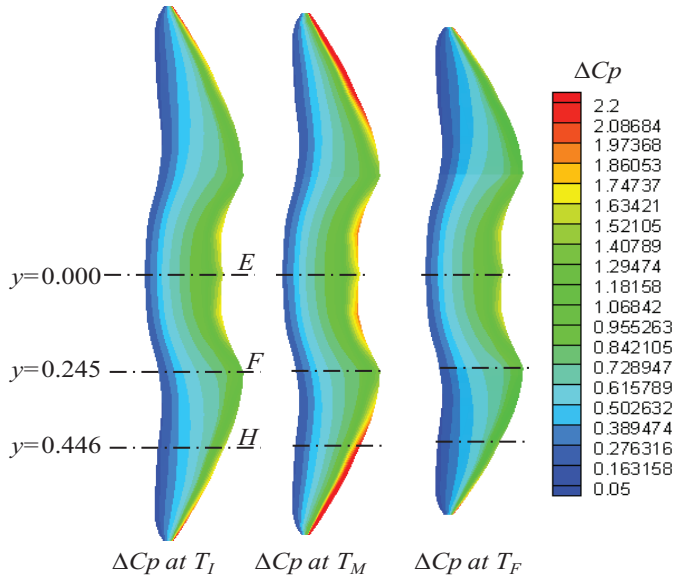

Figure 12: distribution of pressure for case II.

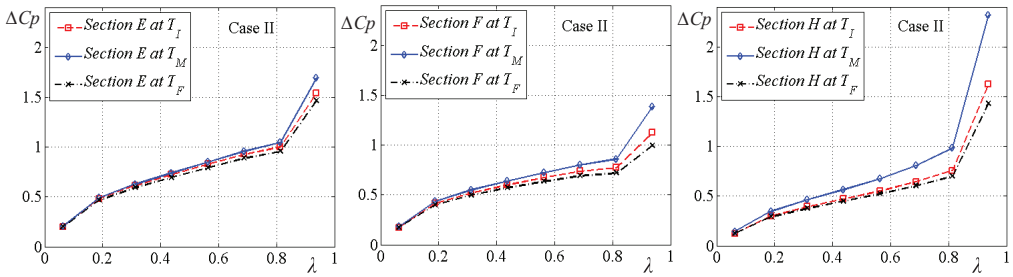

Figure 13: distribution of pressure for case II at sections E, F, and H

At section E, the behavior of ΔC_p is similar in magnitude at the three instants; only a slight difference occurs near the leading edge. At section F, this difference at the leading edge is a little larger, and at section H it is even larger. In all three locations the difference decreases toward the trailing edge where ΔC_p appears to be nearly zero at all times and at all locations, which can be confirmed by analyzing at other times. Thus, the time-dependent behavior near the trailing edge is consistent with the unsteady Kutta condition, which requires ΔC_p to be zero along these edges at all times.

In Figure 14, the wakes are plotted at different instants. In parts *a*, *b* and *c*, the development of the wakes before the morphing process begins is shown. The results show the starting vortex following an impulsive start and the roll up in the wing-tip vortex systems. In parts *d*, *e* and *f*, the wakes are shown after 700 time steps for cases I, II and III, respectively. The results reveal how the wakes adapt to the wing configuration by forming different patterns. These patterns show the wingtip vortices as well as

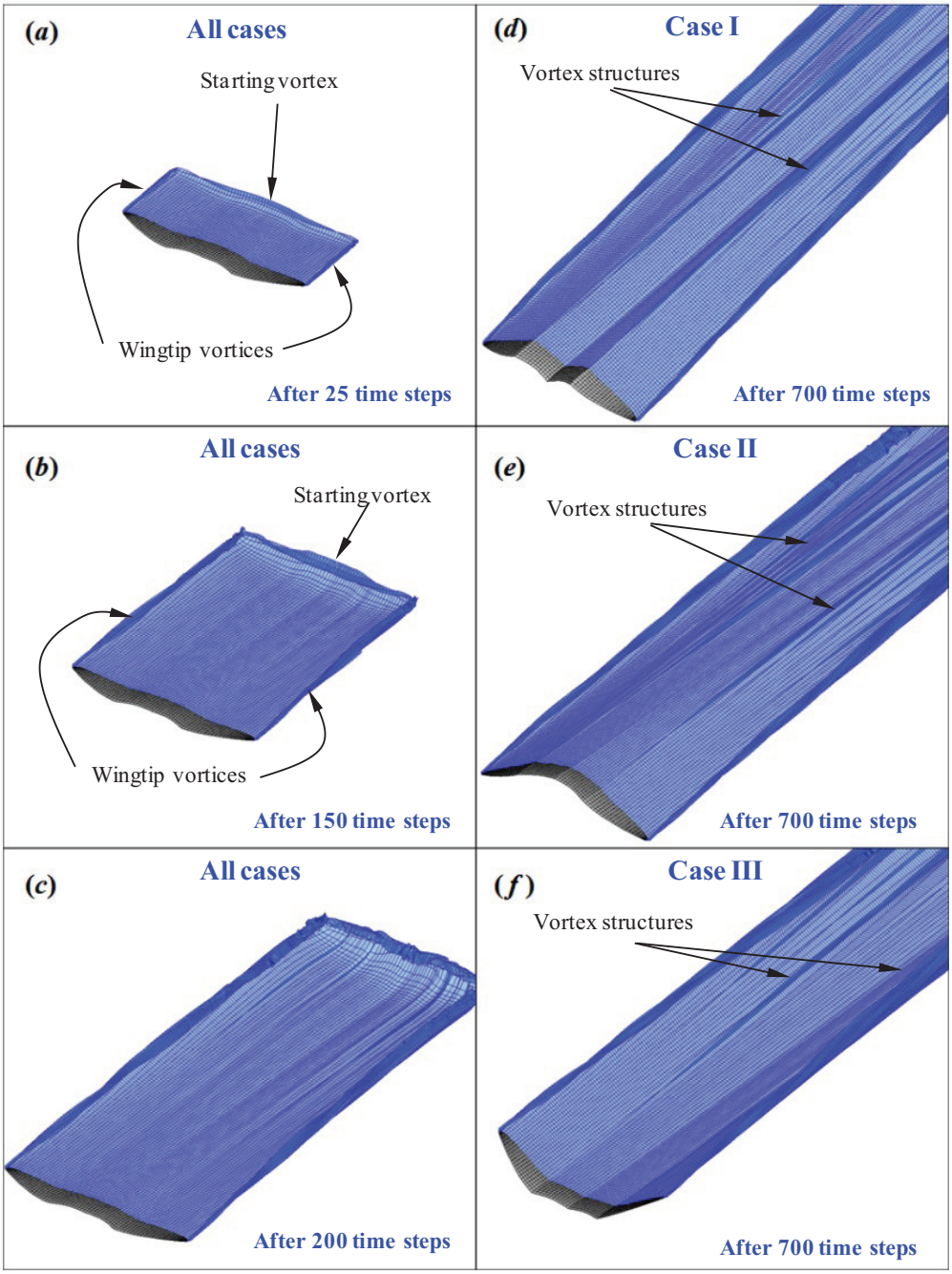

Figure 14: wake evolution.

the existence of other vortex structures associated with abrupt changes in the planform. The vorticity in the wake can significantly alter the fluid flow near the wing, which in turn affects the distribution of vorticity on the wing's surface and, hence, the loads acting on the wings. These results show how UVLM is able to capture the wake's patterns, and hence its influence on aerodynamic characteristics, which could not be captured by using other methods which impose the wake instead of calculating it as part of the solution.

The strength of the vorticity in the wake at any time was determined in the wing's boundary layers previous to being shed; thus the loads now are dependent on what happened earlier. However, as the vorticity in the wake is swept downstream, its influence decreases, as indicated in equation (19). Consequently, the more recent the motion is the stronger its influence is. As a result, the wake generally can be truncated as determined by trial and error. The wakes in the last three parts of Figure 14 are rather long to emphasize their shapes, but they are probably longer than necessary for a reasonably accurate estimate of the loads.

Numerical simulations to complete a full morphing cycle (i.e., when the wing returns to its original shape), including how different prescribed kinematic patterns affect the aerodynamic forces, will be addressed in future work.

5. CONCLUSIONS

The development of a numerical model to study the nonlinear and unsteady aerodynamics on a bioinspired morphing-wing concept was described. To change the wing shape, a folding wing mechanism was implemented. This model included: *i*) a wing topology inspired by gull wings, *ii*) a kinematic model to describe the folding mechanism observed in bird flight, *iii*) and a version of UVLM that models unsteady aerodynamic phenomena.

The model was verified by comparing some present results with those obtained by Neef and Hummel, using a method based on the Euler equations, for a flapping-twisting rectangular wing, a case that involves kinematic and aerodynamic aspects. The lifts predicted showed excellent agreement.

Next a mesh sensitivity analysis was carried out in order to select a suitable grid for the numerical simulations of the morphing gull wing, and a compromise between computational cost and accuracy was obtained.

Some important conclusions can be drawn from the results. The vorticity shed from the gull-wing tips has only a slight influence on aerodynamic characteristics; therefore the portion of the wake associated with the wing tips could be neglected in order to reduce computational cost. The aerodynamic characteristics during the morphing process showed a strong dependence on the prescribed kinematics, which implies that the details of the morphing process cannot be ignored. The results also revealed that the flows adapt as the wing is changing configurations by forming different patterns of vortex structures in the wakes, which significantly affect the aerodynamic loads.

UVLM was shown to be appropriate for preliminary analyses of morphing wings due to being readily adaptable to different wing geometries and morphing processes and to its ability to account for the aerodynamic interaction between the wings and the wakes. Another feature that makes this method appealing is its low computational cost compared with computational fluid dynamics simulations.

The numerical model presented in this paper is a good start towards the development of a valuable tool for understanding the aerodynamic changes that occur during a morphing process. In the future, it will be necessary to combine this model with others that model structural dynamics and control systems. At present, the authors are developing a structural model that includes piezoelectric actuators with the goal of combining it with the aerodynamic model presented in this work.

ACKNOWLEDGMENTS

This work was partly supported by the Consejo Nacional de Investigaciones Científicas y Técnicas, Argentina.

REFERENCES

[1] A.Y.N. Sofla, S.A. Meguid, K.T. Tan and W.K. Yeo, "Shape morphing of aircraft wing: Status and challenges," *Materials and Design*, vol. 31, No. 3, pp. 1284–1292, 2010.

[2] J. C. Gomez and E. Garcia, "Morphing unmanned aerial vehicles," *Smart Materials and Structures*, Vol. 20, no. 10, 16 pp., 2011.

[3] B. Sanders, F. E. Eastep, and E. Foster, "Aerodynamic and Aeroelastic Characteristics of Wings with Conformal Control Surfaces for Morphing Aircraft," *Journal of Aircraft*, vol. 40, No. 1, pp. 94-99, 2003.

[4] D.M. Elzey, A.Y.N Sofla and H. N. G. Wadley, "A bio-inspired, high-authority actuator for shape morphing structures," *Proc. SPIE 5053, Smart Structures and Materials 2003: Active Materials: Behavior and Mechanics*, August 2003.

[5] M. Amprikidis and J. E. Cooper, "Development of Smart Spars for Active Aeroelastic Structures," *In: Proceedings of 44th AIAA/ASME/ASCE/AHS Structures, Structural Dynamics, and Materials Conference*, April 2003.

[6] A. Chakravarthy, D.T. Grant and R. Lind, "Time-Varying Dynamics of a Micro Air Vehicle with Variable-Sweep Morphing," *Journal of Guidance, Control, and Dynamics* Vol. 35, No. 3, pp. 890-903, 2012.

[7] J.S. Bae, T.M. Seigler, and D.J. Inman, "Aerodynamic and Static Aeroelastic Characteristics of a Variable-Span Morphing Wing", *Journal of Aircraft*, Vol. 49, No. 3, pp. 528-534, 2005.

[8] J. Blondeau, J. Richeson and D.J. Pines, "Design, Development and Testing of a Morphing Aspect Ratio Wing Using an Inflatable Telescopic Spar," *In: Proceedings of 44th AIAA/ASME/ASCE/AHS/ASC Structures, Structural Dynamics and Materials Conference*, April 2003.

[9] S. Barbarino, O. Bilgen, R. M. Ajaj, M. I. Friswell and D. J. Inman, "A Review of Morphing Aircraft," *Journal of Intelligent Material Systems and Structures*, vol. 22, no. 9, pp. 823-877, 2011.

[10] C. Thill, J. Etches, I. Bond, K. Potter and P. Weaver, "Morphing skins," *The Aeronautical Journal*, vol. 112, No. 1129, pp. 117-139, 2008.

[11] J. N. Kudva, "Overview of the DARPA Smart Wing Project," *Journal of Intelligent Material Systems and Structures*, vol.15, No. 4, pp. 261-267, 2004.

[12] T.A. Weisshaar, "Morphing Aircraft Technology – New Shapes for Aircraft Design," Unclassified NATO Rept. RTO-MP-AVT-141, 2006.

[13] M. H. Love, P. S. Zink, R. L. Stroud, D. R. Bye, S. Rizk and D. White, "Demonstration of morphing technology through ground and wind tunnel tests," *48th AIAA/ASME/ASCE/AHS/ASC Structures, Structural Dynamics, and Materials,* April 2007.

[14] T. G. Ivanco, R. C. Scott, M. H. Love, S. Zink and T. A. Weisshaar, "Validation of the Lockheed Martin morphing concept with wind tunnel testing,". *48th AIAA/ASME/ASCE/AHS/ASC Structures, Structural Dynamics, and Materials Conference, April* 2007.

[15] D.T. Grant, M. Abdulrahim, and R. Lind, "Flight Dynamics of a Morphing Aircraft Utilizing Independent Multiple-Joint Wing Sweep," *International Journal of Micro Air Vehicles*, vol. 2, No 2, 2010.

[16] M. Abdulrahim and R. Lind, "Flight Testing and Response Characteristics of a Variable Gull-Wing Morphing Aircraft," *AIAA Guidance, Navigation, and Control Conference and Exhibit*, August 2004.

[17] H. Namgoong, W. A. Crossley and Lyrintzis A. S., "Aerodynamic Optimization of a Morphing Airfoil Using Energy as an Objective," *AIAA Journal* Vol. 45, No. 9, pp. 2113-2124, 2007.

[18] B. Obradovic and K. Subbarao, "Modeling of Flight Dynamics of Morphing-Wing Aircraft," *Journal of Aircraft* Vol. 48, No. 2, pp. 391-402, 2011.

[19] I. Wang, S.C. Gibbs, and E. H. Dowell, "Aeroelastic Model of Multisegmented Folding Wings: Theory and Experiment," *Journal of Aircraft*, Vol. 42, No. 2, pp. 911-921, 2012.

[20] Q. Wang, Y. Chen and H. Tang, "Mechanism Design for Aircraft Morphing Wing," *53rd AIAA/ASME/ASCE/AHS/ASC Structures, Structural Dynamics and Materials Conference*, April 2012.

[21] R. De Breuker, M. Abdalla, Z. Gürdal and D. Lindner, "Energy-Based Aeroelastic Analysis of a Morphing Wing," *Proc. SPIE 6523, Modeling, Signal Processing, and Control for Smart Structures*, April 2007.

[22] A. M. Wickenheiser and E. Garcia, "Aerodynamic Modeling of Morphing Wings Using an

Extended Lifting-Line Analysis," *Journal of Aircraft*, Vol. 44, No. 1, pp. 10-16, 2007.

[23] A. Niksch, J. Valasek, T.W. Strganac and L. A. Carlson, "Morphing Aircraft Dynamical Model: Longitudinal Shape Changes," *AIAA Atmospheric Flight Mechanics Conference and Exhibit*, August 2008.

[24] C.O. Johnston, D.A. Neal, L.D. Wiggins, H.H. Robertshaw, W.H. Mason, and D.J. Inman, ''A Model to Compare the Flight Control Energy Requirements of Morphing and Conventionally Actuated Wings,'' *Proceedings of 44th AIAA/ASME/ASCE/AHS Structures, Structural Dynamics, and Materials Conference*, April 2003.

[25] T. Yue, L. Wang and J. Ai, "Multibody Dynamic Modeling and Simulation of a Tailless Folding Wing Morphing Aircraft," *AIAA Atmospheric Flight Mechanics Conference*, August 2009.

[26] S. M. Belotserkovskii, "Study of the Unsteady Aerodynamics of Lifting Surfaces Using the Computer," *Annual Review of Fluid Mechanics*, Vol. 9, pp. 469–494, 1977.

[27] E. H. Atta, O. A. Kandil, D. T. Mook and A. H. Nayfeh, "Unsteady Aerodynamic Loads on Arbitrary Wings Including Wing-Tip and Leading-Edge Separation," AIAA Paper 1977-0156, 1977.

[28] P. Konstandinopoulos, D. F. Thrasher, D. T. Mook, A. H. Nayfeh and L. Watson, "A Vortex-Lattice Method for General Unsteady Aerodynamics," *Journal of Aircraft*, Vol. 22, No. 1, pp. 43–49, 1985.

[29] J. Katz, and A. Plotkin, , *Low-Speed Aerodynamics*, 2nd ed., Cambridge Univ. Press, New York, pp. 421–495, 2001.

[30] Y.Y. Jung, and J.H. Kim, "Unsteady Subsonic Aerodynamic Characteristics of Wing in Fold Motion," *International Journal of Aeronautical and Space Science*, Vol. 12, No. 1, pp 63–68, 2011.

[31] Z. G. Wang, and Z. N. Zhang, "Modeling and Simulation of Unsteady Aerodynamics on a Morphing Wing," *Applied Mechanics and Materials*, Vol. 427-429, pp. 77-80, 2013.

[32] H. Tennekes, *The Simple Science of Flight: From Insects to Jumbo Jets* (Cambridge, Massachusetts: MIT Press), 2009.

[33] T. Liu, K. Kuykendoll, R. Rhew, and S. Jones, "Avian Wing Geometry and Kinematics," *AIAA Journal* Vol. 44, No. 5, pp.954-963, 2006.

[34] M. D. Shuster, "A survey of attitude representations," *The Journal of the Astronautical Sciences*, Vol 41, No. 4, pp. 439-517, 1993.

[35] H. Baruh, *Analytical Dynamics*. McGraw Hill, 1999

[36] S. Preidikman, "Numerical Simulations of Interactions Among Aerodynamics, Structural Dynamics, and Control Systems," Ph.D. Dissertation, Dept. of Engineering Science and Mechanics, Virginia Polytechnic Inst. and State Univ., Blacksburg, VA, 1998.

[37] P. Konstandinopoulos, D. T. Mook, A. H. Nayfeh, "A numerical method for general, unsteady aerodynamics," in: American Institute of Aeronautics and Astronautics: Athmospheric Flight Mechanics Conference, 1981.

[38] M. Neef, and D. Hummel, "Euler Solution for a Finite-Span Flapping Wing," *Fixed and Flapping Wing Aerodynamics for Micro Air Vehicle Applications*, edited by T. J., Muller, Progress in Astronautics and Aeronautics, AIAA, Reston, VA, 2001, Vol. 195, pp. 429–449, Chap. 19.